Journal of Quantitative Spectroscopy & Radiative Transfer 346 (2025) 109588

Contents lists available at ScienceDirect

Journal of Quantitative Spectroscopy and Radiative Transfer

journal homepage: www.elsevier.com/locate/jqsrt

Multi-laboratory measurements of $^{12}CH_4$ $2\nu_3$-band line parameters. Part II: Spectrum analysis based on the speed dependent Voigt profile with first-order line mixing

R.-H. Yin [a], J.-K. Li [a], J. Wang [b], A.-W. Liu [b], Z.D. Reed [c], J.T. Hodges [c], M. Birk [d], Y. Tan [a,b,*], S.-M. Hu [a,b]

[a] Hefei National Research Center for Physical Sciences at the Microscale, University of Science and Technology of China, Hefei, 230026, Anhui, China
[b] Hefei National Laboratory, University of Science and Technology of China, Hefei, 230088, Anhui, China
[c] Chemical Sciences Division, National Institute of Standards and Technology, Gaithersburg, 20889, MD, USA
[d] Remote Sensing Technology Institute, German Aerospace Center (DLR), Wessling, D-82234, Germany

ARTICLE INFO

Keywords:
Methane spectroscopy
Nitrogen broadening
Cavity ring-down spectroscopy
Speed-dependent Voigt profile
1.64 μm window

ABSTRACT

Methane (CH_4), the second most important greenhouse gas, playing a critical role in atmospheric monitoring for global climate change research. The 1.64 μm spectral region (6050–6250 cm^{-1}), corresponding to the $2\nu_3$ vibrational band of methane, is particularly advantageous for remote sensing due to its strong absorption features and minimal interference from water vapor. As a result, wavelengths within this band correspond to a primary detection region for satellite missions such as MERLIN and GOSAT-2. However, current uncertainties in the HITRAN database — particularly in the line-shape parameters of strong lines within the $2\nu_3$ band where discrepancies of 5%–10% persist, limit the precision of atmospheric concentration retrievals. To address this challenge, we employ optical-frequency-comb-referenced cavity ring-down spectroscopy measurements of N_2-broadened methane samples analyzed with the speed-dependent Voigt profile and first-order line mixing. This study provides line-shape parameters line mixing coefficients for the $2\nu_3$ band transitions from R(0) to R(10) at pressures between 10 and 50 kPa. Air-broadened values for these quantities based on scaling rules are also presented for atmospheric applications. Our measurements achieve relative uncertainties of less than 1 %, thereby significantly improving upon prior data archived in the HITRAN2020 database. These results provide essential experimental benchmarks for refining methane spectral databases, thereby enhancing the accuracy of satellite remote sensing and ground-based observations.

1. Introduction

Although the amount fraction of methane (CH_4) in the atmosphere is relatively small, its global warming potential is 28 times greater than that of CO_2, and consequently, it has a large influence on Earth's radiative balance, contributing 23% of anthropogenic greenhouse forcing [1]. The $2\nu_3$ vibrational band near 1.64-μm (6050–6250 cm^{-1}) has emerged as a cornerstone for satellite remote sensing missions including MERLIN [2] and GOSAT-2 [3], owing to its optimal combination of strong CH_4 absorption cross-sections (10^{-22}–10^{-20} cm^2/molecule) and minimal water vapor interference (≤5% absorption contribution). However, the precision in determining atmospheric methane concentrations is hindered by existing uncertainties in the line-shape parameters of the HITRAN spectral database, particularly for the majority of strong lines in the $2\nu_3$ band. Within the existing HITRAN database, the error codes associated with the spectral line shape parameters for these intense absorption spectral lines are assigned '5' and '3'. These codes correspond to error ranges of '5–10%' and 'greater than 20%', respectively. [4,5]. Using the spectroscopic data derived from implementing the commonly used Voigt profile with the HITRAN line list could lead to deviations of up to 2% between the calculated and measured absorption coefficients. This would propagate systematic errors exceeding 1% in total column retrievals [6], which is particularly problematic for the upper tropospheric layers.

Atmospheric models of absorption line-shapes usually rely on Voigt profiles, but recent studies demonstrate their inadequacy for overlapping transitions. Yang et al. [7] showed that more advanced line-shapes like the Hartmann–Tran profile (HTP) significantly reduce residuals for $2\nu_3$ R(9) manifold lines. However, computational complexity limits use

* Corresponding author at: Hefei National Research Center for Physical Sciences at the Microscale, University of Science and Technology of China, Hefei, 230026, Anhui, China.
E-mail address: tanyan@ustc.edu.cn (Y. Tan).

https://doi.org/10.1016/j.jqsrt.2025.109588
Received 29 April 2025; Received in revised form 15 July 2025; Accepted 15 July 2025
Available online 1 September 2025

of the HTP in practice. Additionally, correlation between variables in this spectrally congested region can increase the uncertainty of fitted parameters. The speed-dependent Voigt profile (SDVP) combined with the first-order line-mixing model (LM) provides a pragmatic balance between physical fidelity and computational efficiency, particularly for atmospheric pressure ranges relevant to measurements of tropospheric methane.

The 1.64 μm window is spectrally intricate and challenging to characterize as it is part of the tetradecad polyad, with 30% of its spectral lines remaining unassigned due to the presence of overlapping hot bands and transitions involving high-J levels [3,4,8,9]. Prevailing spectral databases, such as HITRAN2020 [4], are inadequately equipped with empirical constraints necessary for precisely determining line-shape parameters that extend beyond the Voigt profile. This deficiency results in systematic biases in lidar data interpretation [2,10].

In recent years, numerous research groups have focused on enhancing our understanding of the spectral properties of methane. Key spectral parameters for modeling the absorption spectrum include line positions, integrals of cross-sections (i.e. line intensities), and those associated with line-shapes (including widths and pressure-induced shifts). For remote sensing applications, the properties of absorption line-shapes hold significant importance. Inaccurate modeling of line-shapes, arising from uncertainties in spectral broadening parameters or from selecting an unsuitable line profile, frequently results in erroneous gas concentration assessments, manifesting as biases that are latitudinal, seasonal, or regional in nature. As discussed earlier, limitations of traditional line-shape models necessitate the incorporation of more sophisticated parameterized profiles to simulate spectral absorption cross-sections with a precision within 1%.

The latest measurements of line-shape parameters for the CH_4 $2\nu_3$ band can be found in the study by Delahaye et al. [6] and Vasilchenko et al. [11]. There are four relevant works on the absorption spectroscopy of the methane $2\nu_3$ band [12–15], all of which are based on Fourier transform spectroscopy (FTS). Except for the study by Devi et al. [15], the other studies used the Voigt profile (VP) to model the line-shapes of isolated methane transitions. Given that this model cannot reproduce the absorption spectrum to within a few percentage points of accuracy, it is now considered to be outdated in many applications. Furthermore, when modeling observed line-shapes, other pressure-related collision effects such as line mixing, Dicke narrowing, and speed dependence must be considered to more accurately reproduce the measured spectra. Instrument-induced line-shape distortions make the accurate determination of line-shape parameters in traditional FTS challenging. At the same time, because the optical path length used in FTS spectrometers is limited (requiring high-concentration absorbing samples), the contribution of methane self-broadening cannot be ignored, which poses a disadvantage for the accurate determination of air-broadened line-shapes. The most recent absorption spectra measured in the laboratory come from cavity ring-down spectroscopy (CRDS), where frequency-calibrated (FS-CRDS) technology has been applied to line-shape measurements for the CH_4 $2\nu_3$ band. These results, however, are limited to the R(6) and R(9) manifolds [6,7,16].

This manuscript discusses Part II in a set of precise measurements of the methane spectrum near 1.64 μm, with particular emphasis on enhancing the accuracy of line profile parameters. Henceforth, we refer to Part I of this study, i.e. Reed et al. [17], which focuses on line intensities, as the "companion" methane study. Our approach in these two parts involved collaboration with two research teams, one from the United States National Institute of Standards and Technology (NIST) and another from the German Aerospace Center (DLR), to utilize their independent data on line intensities recorded on nearly Doppler-limited spectra recorded at low pressures. Line positions were anchored to the most recent calibrations obtained from optical frequency combs in methane saturation absorption spectroscopy, as reported by Votava et al. (2022) [18]. We adopted intensity ratios derived from the NIST and DLR datasets reported in the companion methane study, while line positions were constrained according to the PCCP 2022 standards [18]. This study showcases a newly developed CRDS system at the University of Science and Technology of China (USTC), featuring both ultra-stable temperatures and precise and accurate pressure calibration. This apparatus facilitated the recording of methane spectra in a matrix of N_2, specifically targeting the R(0) through R(10) manifold region of the $2\nu_3$ band of $^{12}CH_4$ across three pressure points ranging from 10 kPa to 50 kPa. We employed a comprehensive fitting algorithm based on the first-order line mixing (LM) and speed-dependent Voigt profile, which allowed for simultaneous parameter adjustments across all examined pressure conditions. Details of the CRDS experimental arrangement are elucidated in Section 2. Section 3 elaborates on the implementation of the SDV and first-order line-mixing model and presents the N_2-broadening coefficients for these manifolds, benchmarking against HITRAN2020 and other CRDS-based results. Section 4 explores the ramifications of our findings and proposes updates to spectral databases.

2. Experiment

In this study, the laser-locked cavity ring-down spectroscopy (LL-CRDS) technique [19,20] was used for highly accurate and sensitive determination of methane absorption features. Fig. 1 illustrates the experimental arrangement. The experiment employed an external cavity diode laser (ECDL, Toptica) as the light source. The optical cavity included two mirrors with a 99.998% intensity reflectivity, operating over the wavelength range 1.5 to 1.7 μm. The mirror-to-mirror distance in the cavity was approximately 140 cm, corresponding to a free spectral range (FSR) close to 107.28 MHz, while the cavity mode width was about 0.6 kHz. The optical cavity resided within an aluminum chamber, which was temperature-regulated to roughly 298.378 K via a proportional–integral–derivative (PID) controller. Temperatures were measured with platinum resistance thermometers, with temperature fluctuations and deviations between the sensors kept under 6 mK, resulting in a temperature measurement uncertainty of 10 mK, as shown in Fig. 2.

In the experimental configuration, the laser output was bifurcated into two beams utilizing beam splitters: one dedicated to frequency locking and the other for spectral probing. The frequency-locking beam was employed to stabilize the laser frequency against the high-finesse optical resonator via the Pound–Drever–Hall (PDH) technique. Along with meticulous temperature regulation, this process helped maintain cavity length stability, thereby minimizing external perturbations and allowing for accurate, consistent measurements of the absorption spectrum frequency axis. Additionally, a segment of the locking beam was integrated with a frequency comb to calibrate the laser frequency, ensuring stability over extended periods. Prior to entering the optical cavity for ring-down measurements, the probing beam traversed an acousto-optic modulator (AOM) and a fiber-electro-optic modulator (fiber-EOM). The AOM functioned as an optical switch, shutting off the probing light once the cavity output attained a preset threshold. This allowed us to initiate the decay signal, which was subsequently recorded with a digitizer and fit with an exponential function to ascertain the ring-down time. The frequency shift between the spectral and locking beams was precisely modified to coincide with the difference between adjacent cavity mode frequencies. This ensured that the transmitted beam maintained resonance with one cavity mode while the locking beam corresponded with another.

Through modulation of the fiber-EOM frequency, we accomplished rapid and broad frequency scanning exceeding 20 GHz. The scanning intervals were aligned with the free spectral range (FSR) of the ring-down cavity, approximately 107 MHz. Precise regulation of the RF signal source controlling the fiber-EOM was essential for accurate laser frequency assessment. This approach enhanced the CRDS measurement sensitivity and expanded the adaptability of the frequency scanning method. The determination of the spectrum frequency axis

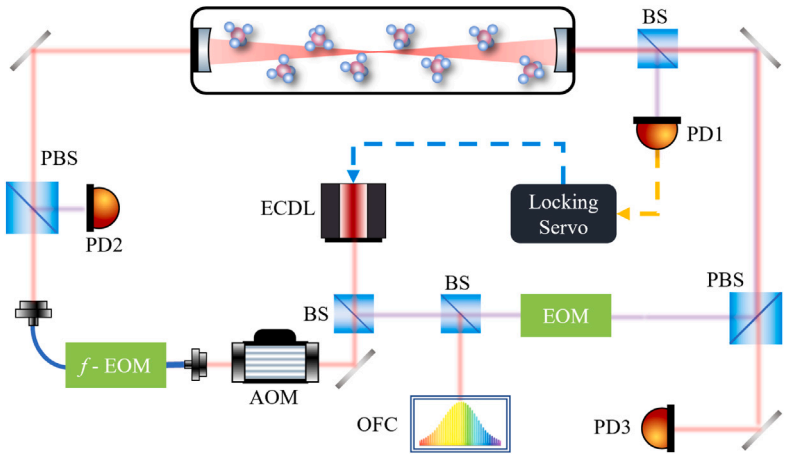

Fig. 1. Experimental setup for CRDS: AOM: Acousto-Optic Modulator, EOM: Electro-Optic Modulators, HWP: Half-Wave Plates, PBS: Polarizing Beam Splitter, BS: Beam Splitter, PD: Photodetector.

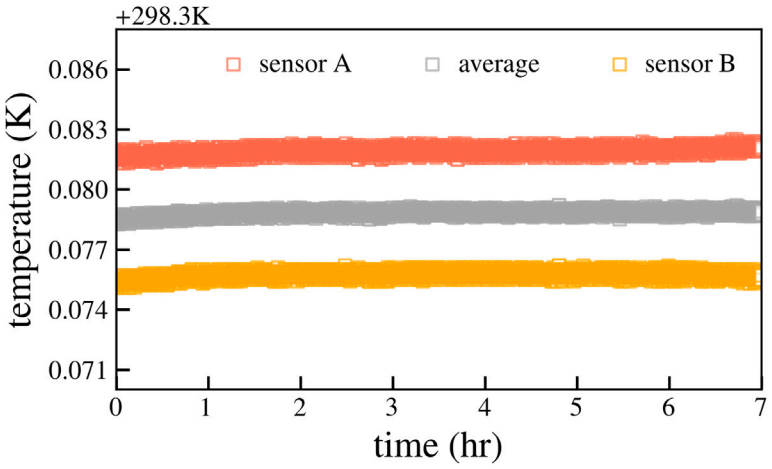

Fig. 2. Cavity temperature drift measured by two 100 Ω platinum resistance thermometers.

(f_{abs}) was anchored to the optical frequency comb (OFC) using the formula provided below:

$$f_{abs} = f_{\text{beat}} + f_0 + N * f_r + f_{\text{AOM}} + f_{\text{EOM}}, \tag{1}$$

where f_{beat} refers to the frequency beat signal from the laser and OFC, f_0 and f_r are the carrier offset frequency and the repetition frequency of the OFC, f_{AOM} denotes the frequency shift from the AOM, and f_{EOM} represents the shift due to the fiber-EOM. This integrated strategy enabled precise frequency calibration with extensive tuning potential.

Following extinction of the spectral beam, the decaying transmitted beam intensity was recorded. This procedure enabled the determination of the absorption coefficient for the gas sample inside the cavity, at the laser beam's specific frequency, using the subsequent equation:

$$\alpha = \frac{1}{c}\left(\frac{1}{\tau_{\text{gas}}} - \frac{1}{\tau_{\text{empty}}}\right) \tag{2}$$

where c denotes the speed of light, τ_{gas} represents the decay time with the gas present, and τ_{empty} is the decay time for an empty cell. The initial laser power was around 4.5 mW, yielding a transmittance of roughly 30%. The evaluation of the system sensitivity involved uninterrupted monitoring over the course of two hours. Analysis of the resulting Allan variance revealed that the system achieved an optimal detection sensitivity of 2.5×10^{-12} cm^{-1}, with an integration time of 30 s (see Fig. 3).

The methane gas sample employed in the experiment was obtained from the National Institute of Metrology, China. This gas possessed a standard methane concentration of 2 ppm, where methane was blended with nitrogen, and exhibited an uncertainty rate of 0.25%. The principal data concerning line strength obtained from the companion study were sourced chiefly from NIST and DLR. At DLR, Fourier Transform Spectroscopy (FTS) was conducted using highly pure methane samples (99.9995% purity). In contrast, the more sensitive Cavity Ring-Down Spectroscopy (CRDS) experiments conducted at NIST and USTC required the use of methane diluted in nitrogen. Given that the methane amount fraction uncertainty for NIST samples was 0.012%, the intensities recorded in NIST's manifold were employed to refine the initial assessment of methane levels in the CRDS spectra acquired at USTC. The pressure of the gas sample was measured using a commercial capacitance manometer, specifically the Leybold CTR101N, for readings below 1000 Torr. Calibration of the Leybold gauge was performed against an Inficon reference manometer, which carries an uncertainty of 3×10^{-5}, multiple times throughout the year, encompassing our experimental period. The deviations are illustrated in Fig. 6(B) of the previously published study by Liang et al. [23]. We adopted the standard deviation, 1.2×10^{-4}, as the uncertainty in our pressure measurements.

In our study, a real-time recording technique was applied for the calibration of frequencies during spectral scanning. This involved capturing the beat frequency between the laser and an optical frequency comb to allow for immediate calibration of the frequency being scanned. The entire spectral scanning action spans roughly 10 s to capture one spectrum, during which a drift of 2.5 kHz in f_{beat} is observed. The

Table 1
Summary of line-shape-parameters for the R(0)–R(10) manifolds, retrieved from SDV profile with N_2 as the buffer gas.

Line[a]	Assignment[b]		SDV and first-order line mixing parameters[c]				
	$J'C'\alpha'$	$J''C''\alpha''$	γ_0	δ_0	γ_2	δ_2	y
R0-1	1A2	0A1 1	0.06297(1)	−0.01221(1)	0.00942(3)	−0.00035(3)	0
R1-1	2F2	1F1 1	0.06864(1)	−0.01070(1)	0.00952(2)	−0.00057(3)	0
R2-1[d]	3E	2E 1	0.06635(6)	−0.01630(7)	0.00998(1)	0.00023(2)	0
R2-2[d]	3F1	2F2 1	0.06626(4)	−0.00878(3)	0.00966(2)	0.00062(2)	0
R3-1	4F2	3F1 1	0.06700(5)	−0.01050(2)	0.00956(2)	−6e−0500(6)	0.172(2)
R3-2	4F1	3F2 1	0.06127(4)	−0.01050(2)	0.006127(4)	−6e−0500(6)	−0.172(2)
R3-3	4A1	3A2 1	0.06410(1)	−0.01025(2)	0.00954(2)	−0.00126(3)	0
R4-1	5A2	4A1 1	0.06447(3)	−0.01222(4)	0.01009(3)	−0.00054(6)	0
R4-2	5F2	4F1 1	0.0631(1)	−0.01146(5)	0.00631(1)	−0.00091(4)	0.269(7)
R4-3	5E	4E 1	0.058878(1)	−0.0057(2)	0.00943(3)	−2e−0500(F)	0
R4-4	5F1	4F2 1	0.06564(5)	−0.01146(5)	0.01014(5)	−0.00091(4)	−0.269(7)
R5-1	6F2	5F1 1	0.06362(3)	−0.01379(1)	0.00832(2)	−0.00169(4)	0.241(4)
R5-2	6F1	5F2 1	0.07190(6)	−0.01379(1)	0.01281(1)	−0.00169(4)	0.347(4)
R5-3	6E	5E 1	0.05349(3)	−0.00716(4)	0.00747(2)	0.00157(4)	0
R5-4	6F2	5F1 2	0.07140(4)	−0.01379(1)	0.00924(2)	−0.00169(4)	−0.588(1)
R6-1	7E	6E 1	0.05822(6)	−0.01379(5)	0.00940(−)	−0.00018(3)	0
R6-2	7F1	6F2 1	0.06335(9)	−0.01001(3)	0.008255(8)	−0.00080(4)	0.256(2)
R6-3	7A1	6A2 1	0.06349(2)	−0.01047(5)	0.01116(1)	−0.00216(6)	0.233(1)
R6-4	7F1	6F2 2	0.06176(2)	−0.01001(3)	0.00938(4)	−0.00080(4)	0.525(2)
R6-5	7F2	6F1 1	0.05559(8)	−0.01001(3)	0.005559(8)	−0.00080(4)	−0.781(1)
R6-6	7A2	6A1 1	0.06466(3)	−0.01047(5)	0.011436(8)	−0.00216(6)	−0.233(1)
R7-1	8F2	7F1 1	0.05795(2)	−0.011192(6)	0.00885(1)	−0.00019(1)	0.198(3)
R7-2	8F1	7F2 1	0.06188(2)	−0.011192(6)	0.00873(2)	−0.00019(1)	−0.054(3)
R7-3	8A1	7A2 1	0.057989(7)	−0.01170(1)	0.00983(−)	−0.00155(3)	0
R7-4	8F1	7F2 2	0.06444(2)	−0.011192(6)	0.006444(2)	−0.00019(1)	0.4310(7)
R7-5	8E	7E 1	0.04759(2)	−0.00999(2)	0.009518(4)	−0.00030(2)	0
R7-6	8F2	7F1 2	0.063681(9)	−0.011192(6)	0.00999(1)	−0.00019(1)	−0.5757(6)
R8-1	9A2	8A1 1	0.04863(2)	−0.00909(2)	0.006193(7)	0.00031(2)	0
R8-2	9F2	8F1 1	0.05858(6)	−0.01392(1)	0.005858(6)	−0.002227(9)	0.125(1)
R8-3	9E	8E 1	0.06810(4)	−0.01469(2)	0.00972(−)	−0.002612(7)	−0.117(2)
R8-4	9F1	8F2 1	0.058785(6)	−0.01392(1)	0.009842(8)	−0.002227(9)	−0.0118(3)
R8-5	9F2	8F1 2	0.06302(1)	−0.01392(1)	0.00923(2)	−0.002227(9)	0.4703(3)
R8-6	9E	8E 2	0.05032(2)	−0.01469(2)	0.008191(4)	−0.002612(7)	0.117(2)
R8-7	9F1	8F2 2	0.06442(1)	−0.01392(1)	0.01040(−)	−0.002227(9)	−0.583(1)
R9-1[d]	10F2	9F1 1	0.05122(2)	−0.0221(3)	0.007107(9)	−0.00081(4)	0.106(1)
R9-2[d]	10F1	9F2 1	0.05285(2)	−0.0221(3)	0.010570(4)	−0.00081(4)	−0.068(2)
R9-3[d]	10E	9E 1	0.05132(5)	−0.0198(3)	0.01026(1)	0.00086(2)	0
R9-4[d]	10F2	9F1 2	0.07098(F)	−0.0221(3)	0.00710(F)	−0.00081(4)	0.148(1)
R9-5[d]	10A2	9A1 1	0.05488(1)	−0.0210(3)	0.005488(1)	0.00141(4)	0.1253(7)
R9-6[d]	10F2	9F1 3	0.05871(1)	−0.0221(3)	0.00859(−)	−0.00081(4)	0.6466(9)
R9-7[d]	10F1	9F2 2	0.05444(2)	−0.0221(3)	0.005444(2)	−0.00081(4)	−0.8336(4)
R9-8[d]	10A1	9A2 1	0.05775(1)	−0.0210(3)	0.005775(1)	0.00141(4)	−0.1253(7)
R10-1[e]	11E	10E	0.04633(1)	−0.00895(2)	0.004633(1)	−0.00163(1)	−0.1185(6)
R10-2[e]	11F2	10F1	0.04492(2)	−0.01691(1)	0.004492(2)	−0.003107(4)	0.651(−)
R10-3[e]	11A2	10A1	0.06120(3)	−0.01972(2)	0.006120(3)	−0.003249(2)	−0.1265(9)
R10-4[e]	11F2	10F1	0.06274(2)	−0.01691(1)	0.006274(2)	−0.003107(4)	0.4662(9)
R10-5[e]	11F2	10F1	0.06439(1)	−0.01691(1)	0.006439(1)	−0.003107(4)	0.4000(5)
R10-6[e]	11?	10?	0.03954(F)	−0.014873(9)	0.00395(F)	0.00170(1)	0
R10-7[e]	11E	10E	0.04979(2)	−0.00895(2)	0.004979(2)	−0.00163(1)	0.1185(6)
R10-8[e]	11A1	10A2	0.06071(1)	−0.01972(2)	0.006071(1)	−0.003249(2)	0.1265(9)
R10-9[e]	11F2	10F1	0.065589(9)	−0.01691(1)	0.00656(−)	−0.003107(4)	−0.5641(3)
R10-10[e]	11F1	10F2	0.06062(4)	−0.01691(1)	0.006062(4)	−0.003107(4)	−0.4281(6)
R10-11[e]	11F1	10F2	0.06499(1)	−0.01691(1)	0.006499(1)	−0.003107(4)	−0.5247(3)

Notes: Uncertainties in parentheses represent 1-σ statistical errors in the last digit. For example, 0.0664(2) indicates 0.0664 ± 0.0002. (F) denotes an unestimated uncertainty, while (−) indicates an uncertainty too small to report.

[a] Line indices from Votava et al. [18].

[b] Assignments of transitions: $J'C'\alpha'$ for upper states and $J''C''\alpha''$ for lower states, sourced from HITRAN2020, except for R(10).

[c] Parameters retrieved using the SDV and first-order line mixing model: γ_0 and δ_0 are pressure-broadening and shift coefficients ($cm^{-1}atm^{-1}$),γ_2 and δ_2 are speed-dependent broadening and shift coefficients ($cm^{-1}atm^{-1}$), and y are first-order line-mixing coefficients (atm^{-1}).

[d] Data not referenced to the optical frequency comb: 10 kPa and 20 kPa for R(2), and 50 kPa for R(9). Additional free parameters were included to account for frequency shifts, likely increasing δ_0 uncertainties beyond the reported values.

[e] Preliminary assignments based on Nikitin et al. [21], MARVEL [22] and saturation dip values.

data processing employs the mean frequency during this interval as the representative beat frequency, yielding a 1.3 kHz uncertainty for each spectrum. The uncertainties concerning both f_{EOM} and f_{AOM} are relatively minor. All reference sources were synchronized utilizing a rubidium clock disciplined by GPS, providing a long-term stability of 10^{-12}. Meanwhile, stabilization of the optical frequency comb was achieved with a hydrogen maser, exhibiting a fractional frequency drift rate below 3×10^{-16}/day, thereby restricting the repetition rate f_r uncertainty to under 10^{-13}. With these considerations, the total uncertainty in frequency calibration identified in this study is estimated to be within several kilohertz.

3. Method

Spectrum model

The fact that the Voigt profile does not incorporate velocity-dependent collisional effects leads to limitations of this profile which

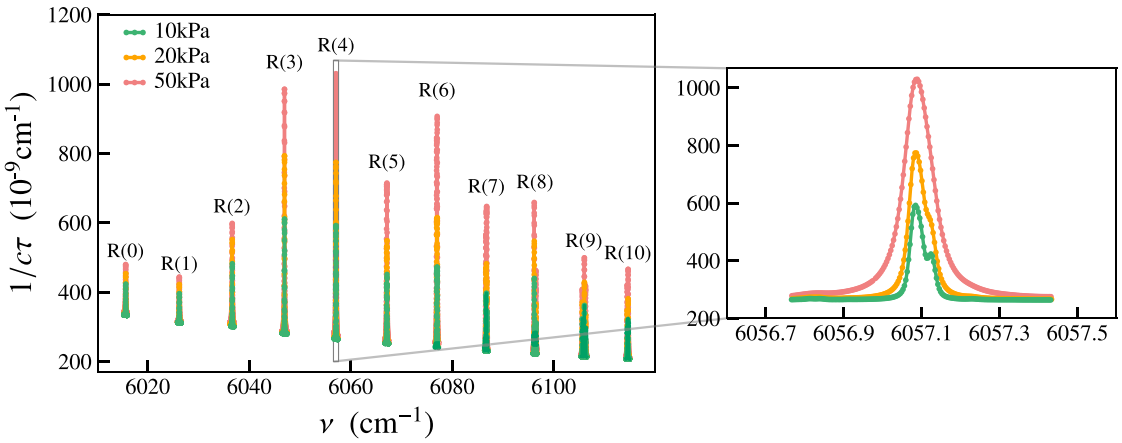

Fig. 3. Spectra recorded at different pressures (10 kPa, 20 kPa and 50 kPa) at room temperature for a mixture with a CH_4 amount fraction of 2 μmol mol^{-1}.

have been extensively validated through laboratory experiments [6,7,16,24]. To achieve a more accurate spectral model for methane, two critical phenomena must be considered: the speed-dependent parameter, which accounts for the modulation of collisional relaxation rates by molecular velocity distributions [25–27], and the line-mixing effect that involves quantum interference between nearby transitions particularly at increased pressures. [28,29] The Hartmann–Tran (HT) profile uses eight physical parameters to model speed-dependent (and other) effects, as described in Refs. [26,27]. However, this high number of fitting parameters—combined with the complexity of methane spectra—often results in strong correlations among spectral line parameters. This is particularly problematic for the highly coupled multi-line spectra of the methane $2\nu_3$ band, where overfitting can lead to inaccurate fits and unphysical results.

The speed dependent Voigt (SDV) profile (which is a reduced form of the HT profile) accompanied by first-order Rosenkranz line-mixing presents an effective solution, requiring only the introduction of two new parameters beyond the Voigt profile ($a_w = \gamma_2/\gamma_0$ or γ_2 for the speed-dependent width; and $a_s = \delta_2/\delta_0$ or δ_2 for shifting parameters) while achieving residuals of less than 1%. Below we verify that the SDV with first-order line mixing over the pressure range of 10 kPa–50 kPa at room temperature provides a precise and predictive model for quantifying the observed spectra, which is essential for monitoring methane within the atmospheric boundary layer. To model line mixing, we used the first-order Rosenkranz line mixing parameter Y [28] and the imaginary component of the complex-valued SDV. From a computational perspective the line mixing parameter is strongly correlated with the line intensity S. Thus, the independent line intensity measurements obtained in the low-pressure domain were indispensable in obtaining reliable line-mixing parameters. With these intensity measurement from NIST and DLR (see companion methane study) providing robust constraints, we implemented a global fit procedure which accounted for speed dependence and line mixing effects.

The absorption coefficient, $\alpha(\nu)$ obtained by CRDS measurements of the observables $(\frac{1}{c\tau(\nu)} - \frac{1}{c\tau_0(\nu)})$ was modeled by writing the spectrum as a sum of manifold (man) lines, background (BG) lines and a linear spectrum baseline (BL) as follows:

$$\alpha(\nu) = \sum_i \alpha_{\mathrm{man},i}(\nu) + \sum_j \alpha_{\mathrm{BG},j}(\nu) + \alpha_{BL}(\nu), \tag{3}$$

where i and j index the individual transitions in the manifold and background, respectively. For each line in the manifold, we account for absorption of the isolated line and line mixing using the complex-valued speed dependent Voigt profile, $\tilde{\Phi}_{\mathrm{SDV}}(\nu;\mathbf{x}_{\mathrm{SDV}})$, to give

$$\alpha_{\mathrm{man},i}(\nu) = n_{CH4} S_i[\tilde{\Phi}^R_{\mathrm{SDV},i}(\nu;\mathbf{x}_{\mathrm{SDV}}) + Y_i\tilde{\Phi}^I_{\mathrm{SDV},i}(\nu;\mathbf{x}_{\mathrm{SDV}})], \tag{4}$$

where $\tilde{\Phi}^R_{\mathrm{SDV},i}$ and $\tilde{\Phi}^I_{\mathrm{SDV},i}$ denote the real and imaginary parts of $\tilde{\Phi}_{\mathrm{SDV}}(\nu;\mathbf{x}_{\mathrm{SDV}})$, correspondingly, where $\mathbf{x}_{\mathrm{SDV}}$ is the vector of parameters for this line profile (see below), and in which n_{CH4} is the number density of methane, S_i is the line intensity and Y_i is the first-order Rosenkranz line mixing coefficient of transition i. Each BG methane line is modeled as a Voigt profile, $\Phi_{\mathrm{V},j}(\nu;\mathbf{x}_{\mathrm{V}})$, with parameter vector $\mathbf{x}_{\mathrm{V}}$, so that the absorption is simply

$$\alpha_{\mathrm{BG},j}(\nu) = n_{\mathrm{CH4}} S_j \Phi_{\mathrm{V},j}(\nu;\mathbf{x}_{\mathrm{V}}), \tag{5}$$

in which we have omitted the line mixing term and where $\Phi_{\mathrm{V}}(\nu;\mathbf{x}_{\mathrm{V}})$ is the real component of the complex-valued Voigt profile. We note that Φ^R_{SDV} and Φ_{V} are each normalized to give unity area upon integration over all frequencies so that $\int_{-\infty}^{\infty}\Phi_{\mathrm{V}}(\nu)d\nu = \int_{-\infty}^{\infty}\tilde{\Phi}^R_{\mathrm{SDV}}(\nu)d\nu = 1$.

In addition, the absorption cross-section, $\sigma(\nu)$, for each line is given by the product $S(T)\tilde{\Phi}^R_{\mathrm{SDV}}$, where $S(T)$ is the line intensity at the measured sample temperature, T. Similarly, the line area for each manifold line is, $n_{\mathrm{CH4}}S(T)$, with analogous expressions for the BG lines.

We also point out (as discussed below) that within a given manifold, because the line intensities were constrained to those given by the companion methane study, all other intensities could be expressed relative to that of the most intense line, S_{max}. In this way, the spectrum analysis based on Eqs. (4) and (5) became independent of n_{CH4} (assuming temperature and pressure were constant for all lines within a given manifold), and consequently S_i/S_{max} and S_j/S_{max} were the only required model inputs that involved intensity. It is worth noting that because all $2\nu_3$ lines within each manifold had the same temperature dependence, it was not necessary to temperature correct (to the experimental conditions) those intensity ratios from the companion methane study, whereas the small number of background intensity ratios, $S_j(T)/S_{\mathrm{max}}$ which were allowed to vary in the fitting algorithm, were corrected for variations in temperature dependence.

Multispectrum global fit method

We applied the multispectrum global fit method to reduce the correlations between fitted parameters used in modeling the absorption spectra of overlapping transitions. The core idea is to concurrently fit spectra obtained at different pressures, p, while constraining five of the spectroscopic parameters given below to be proportional to this quantity.

The parameter set of the SDV profile is $\mathbf{x}_{\mathrm{SDV}} = [\nu_0, \Gamma_{\mathrm{D}}, \Gamma_0, \Delta_0, \Gamma_2, \Delta_2]$, in which the respective quantities (all in frequency or wavenumber dimensions) are zero-pressure line center, Doppler width, Lorentzian width, pressure shift, speed dependence of broadening, and speed dependence of shifting. Also, to account for line mixing in the manifold, the coefficient Y is an additional required parameter. In the evaluation of the Voigt profile, the speed dependence terms are absent and the parameter set is $\mathbf{x}_{\mathrm{V}} = [\nu_0, \Gamma_{\mathrm{D}}, \Gamma_0, \Delta_0]$.

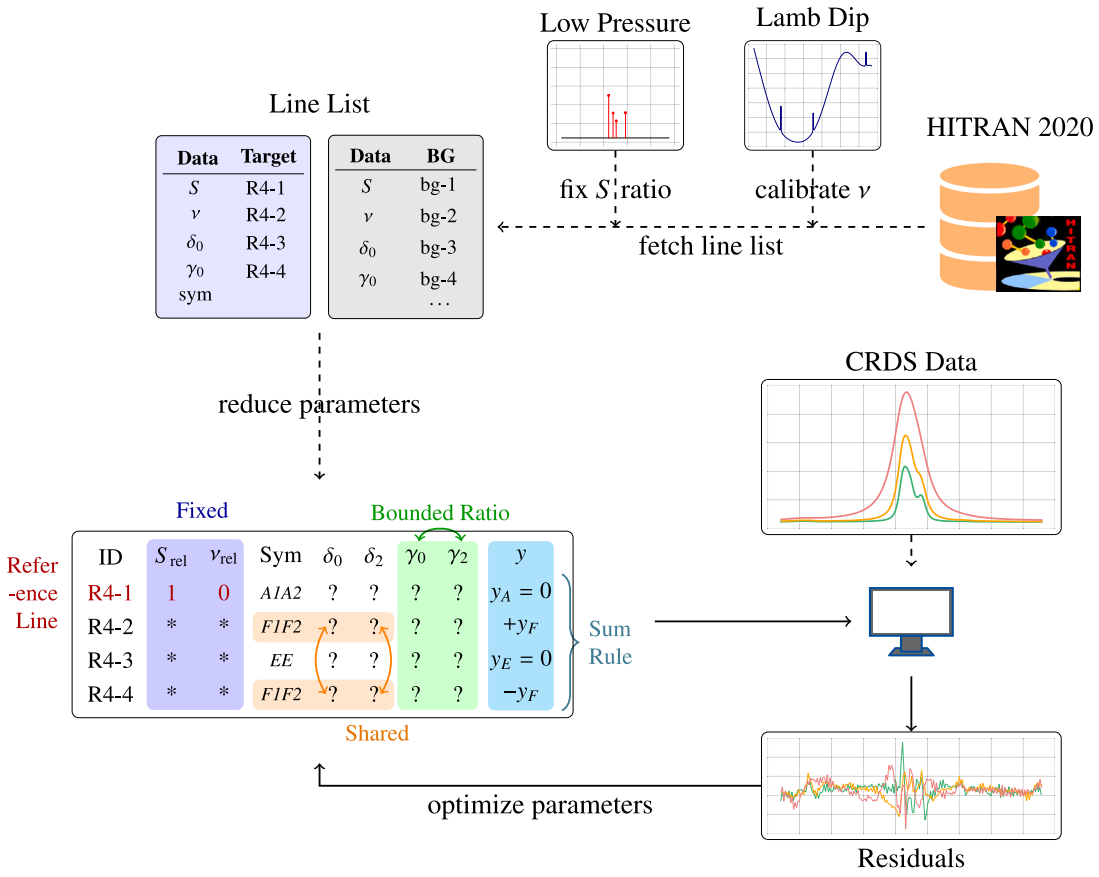

Fig. 4. Diagram of fitting process (R(4) manifold, for example). The process begins by retrieving a list of spectral lines and essential parameters from HITRAN2020. Center frequencies for all lines are then based on prior saturation dip results, yielding the processed line list (upper right). A minimal set of free parameters are then resolved (shown in the lower table). R4-1 is designated as the reference (marked in red). Center frequencies and intensities are converted to relative values (ν_{rel}, S_{rel}) with respect to R4-1 and fixed using saturation dip results (Votava et al.) and low-pressure measurements (Reed et al. which is the outcoming methane paper part I) (purple area). First-order line mixing coefficients (y) are constrained to sum to zero to satisfy the sum rule (light blue area). The ratio of γ_2 to γ_0 is restricted within an empirical range ($0.1 \sim 0.2$) to prevent unphysical results (green area). The shift parameters δ_0 and δ_2 are shared between R4-2 and R4-3, as they belong to the same symmetry species (F1F2) (orange area). The reduced parameter set is then used to generate predicted spectra at various pressures. The difference between the predicted and measured spectra is minimized to determine the optimal parameters.

The multispectrum global fitting procedure involved a coupled analyses on sets of three spectra acquired at pressures of 10 kPa, 20 kPa and 50 kPa. With the assumption that $\Gamma_0, \Delta_0, \Gamma_2, \Delta_2$ and Y are all proportional to p, each line profile was modeled using the measured pressure and the line-by-line pressure-normalized coefficients given by $\gamma_0 = \Gamma_0/p$, $\delta_0 = \Delta_0/p$, $\gamma_2 = \Gamma_2/p$, $\delta_2 = \Delta_2/p$, and $y = Y/p$. For the Voigt profiles which were used to model the BG lines, only γ_0 and δ_0 were required. The transition frequencies were assigned to prior values (as described below), and the Doppler widths, Γ_{D}, were calculated based on the measured sample temperature, transition frequency and molecular mass. The model predictions were then combined and adjusted by least-squares minimization of the global (obs.- calc.)^2 fit residuals. This sharing of pressure-normalized parameters between the spectra acquired at different pressures constitutes a set of robust constraints in the fitting process.

Excluding constants and specific experimental conditions, there are five fitted parameters for each target manifold line: γ_0, δ_0, γ_2, δ_2, and y; whereas each background line requires two fitted parameters: γ_0 and δ_0. The introduction of additional constraints on γ_2, δ_0, δ_2, and y is discussed below.

Step-by-step description of multispectrum global fit procedure

A flowchart of the global fit procedure for the R(4) manifold is shown in Fig. 4. The process begins by querying the HITRAN2020 database to generate a list of relevant transitions along with the required parameters. For this manifold, fifteen spectral lines are selected, with center wavenumbers ranging from 6056.64134 cm^{-1} to 6057.53271 cm^{-1}. Each transition is characterized by its center frequency (ν_0), relative line intensity (S/S_{max}), pressure shifting coefficient (δ_0), line broadening coefficient (γ_0), and assignment information.

Four lines in this set are chosen as target transitions with the strongest line designated as the reference transition for specifying the relative positions within the manifold. The center frequencies of these target transitions are set equal to those reported by Votava et al. [18], which are based on highly accurate (1 kHz uncertainty level) saturation dip spectroscopy position measurements, while the corresponding line intensities are replaced by the low-pressure values reported in the companion methane study Reed et al. [17]. The remaining eleven lines, which are significantly weaker than the target lines, are classified as background (BG) transitions. The center frequencies of these background transitions are first expressed as relative values with respect to the reference line and subsequently converted to absolute frequencies using the results of Ref. [18].

To streamline the optimization process, the parameters of the target lines are systematically reduced to a minimal set. First, center frequencies and line intensities are expressed as relative values (ν_{rel} and $S_{\mathrm{rel}} = S/S_{\mathrm{max}}$) with respect to the reference line; these values remain fixed during the fitting procedure, although the total intensity of the target lines is allowed to vary. Second, the first-order line mixing coefficients are constrained such that their sum is zero, ensuring compliance with the sum rule [29]. Third, to prevent the occurrence of unphysical results, the ratio of γ_2 to γ_0 is constrained to fall within the range ($0.1 \sim 0.2$), which is justified based on prior empirical observations. Lastly, the pressure shift parameters, δ_0 and δ_2, are shared among

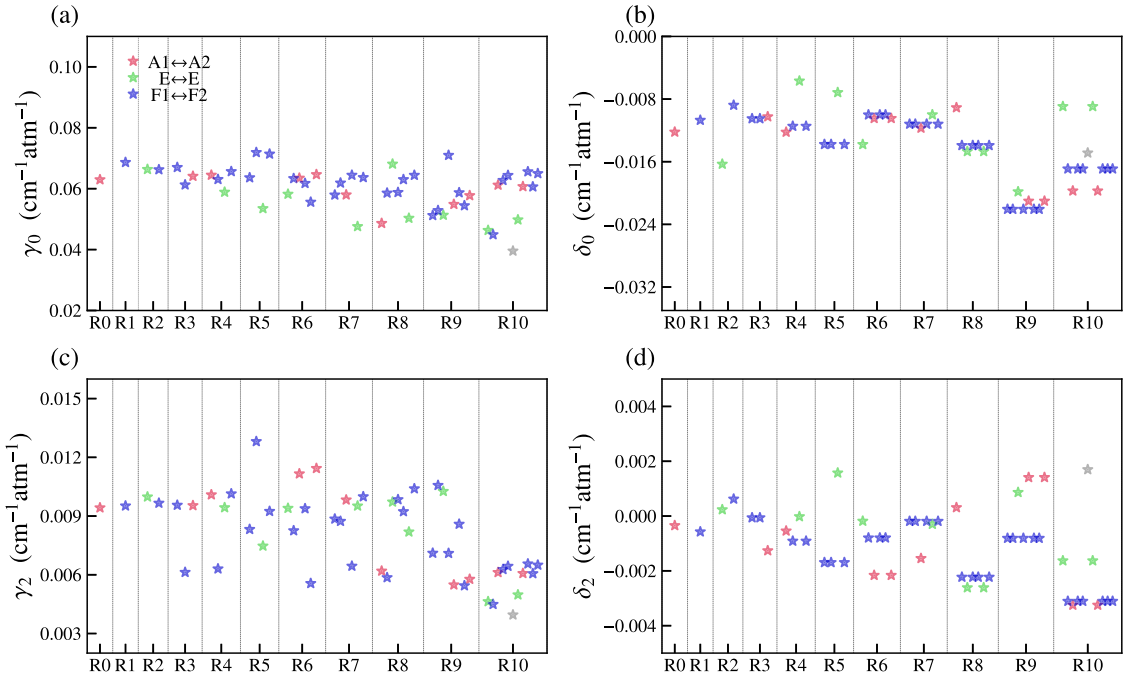

Fig. 5. Pressure broadening (γ_0) and shift (δ_0) coefficients, and speed-dependent broadening (γ_2) and shift (δ_2) coefficients for R(0)-R(10) manifolds (cm^{-1}atm^{-1}, 298 K, N_2 buffer gas). Colors indicate transition symmetries: red (A1↔A2), blue (F1↔F2), green (E↔E).

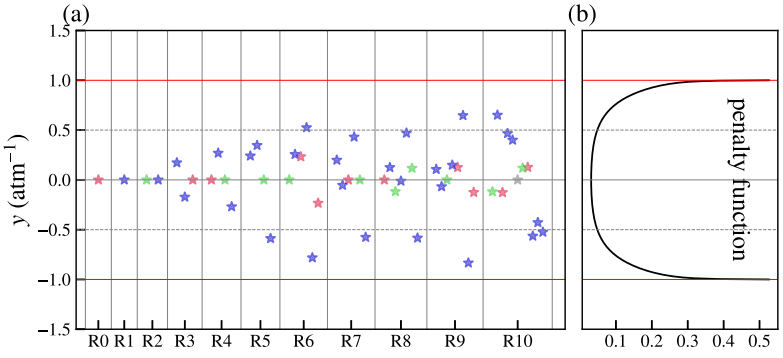

Fig. 6. (a), First-order line-mixing coefficients y (atm^{-1}) for R(0) to R(10) manifolds. (b), Penalty function applied to y during optimization, ensuring y values remain within the range $[-1, 1]$atm^{-1}. The red lines indicate the boundaries of this range.

transitions belonging to the same symmetry species, further reducing the number of free parameters. In the case of the R(4) manifold, The R(4)-2 and R(4)-4 transitions share the same shift parameters. The BG line parameters are generally excluded from the optimization process, except for specific transitions within the R(2), R(8), and R(10) manifolds. Instead, the BG contributions are computed using predefined parameters and subtracted from the spectrum to isolate the target transitions.

The reduced parameter set is then used to generate predicted spectra at three different pressures (10 kPa, 20 kPa, and 50 kPa). The residuals between the predicted and measured spectra are concatenated and fed into the optimization algorithm, which iteratively adjusts the parameters to minimize these residuals.

4. Results and discussion

In this section we report the N_2-broadening (γ_0) and shift (δ_0) coefficients, speed-dependent broadening (γ_2) and shift (δ_2) coefficients, and first-order line mixing coefficients (y) for 53 lines in the R(0) to R(10) manifolds of the $2\nu_3$ band of $^{12}CH_4$. The results are summarized in Table 1. Transition indices and positions ν follow the work of Votava et al. [18]. The assignments for the R(0) to R(9) manifolds are taken from the HITRAN2020 database, whereas the R(10) manifold was previously unassigned in HITRAN. In this study, we aim to integrate various line sources from theoretical predictions by Nikitin et al. [21] and empirical energy levels provided by MARVEL [22]. These results are then compared to saturation-dip-based line position values, resulting in a preliminary assignment for R(10), marked with a dagger (†) in Table 1. As outlined in our previous global fitting methodology, these assignments were crucial in evaluating the constraints based on symmetry-type, thus enabling the production of reliable fit results. The intensities in the fitting procedure are omitted from the accompanying table, because as discussed in Section 2 they were constrained to those given in Reed et al. [17](methane Part I companion paper).

For each manifold, approximately 100 spectra were recorded at pressures of 10 kPa, 20 kPa, and 50 kPa. Figs. 8, 9, and 10 show the fit results for one individual spectra. In Table 1, results from 100 independent fits—to derive the parameter estimations and their statistical uncertainties. A detailed uncertainty analysis is provided in the following subsection.

The fitting process included specific constraints: γ_2/γ_0 was limited to $0.1 \sim 0.2$; the sum of the y coefficients was set to zero; and both δ_0 and δ_2 were constrained to be equal for transitions of the same

symmetry species within each manifold. The results for the R(2) and R(9) manifolds are marked with an asterisk (*) in Table 1, because the data for these transitions (10 kPa and 20 kPa for R(2) and 10 kPa for R(9)) were not calibrated using the optical frequency comb because of some experimental issues.

Figs. 5 and 6 provide a visual summary of all fitted line-shape parameters in Table 1. For γ_0, δ_0, γ_2 and δ_0, the symmetries of the transitions are marked with different colors in Fig. 5 because they are utilized in sharing the δ_0 and δ_2 parameters during the global fit procedure, see Fig. 5(b) and (d). No clear patterns are observed for both broadening coefficients nor shift coefficients versus the lower state rotational quantum number J''. In Fig. 5(c), the γ_2 values are rather randomly scattered within a certain range. This is because γ_2/γ_0 was constrained to be within the range 0.1 to 0.2 boundary during the fitting process, to maintain physicality in the results. Thus the mean value of γ_2 could be a characteristic value for other transitions in the $2\nu_3$ band of methane.

Fig. 6(a) shows the fitted results of the first-order line-mixing parameter. In addition to the previously mentioned sum rule, we imposed a boundary condition of $y \in [-1, 1]\,(\mathrm{atm}^{-1})$ (indicated by the red lines) to ensure that the magnitude of the dispersion term remains smaller than that of the absorption term (see Eq. (4)). This constraint ensures the physical plausibility of the retrieved absorption cross-sections under atmospheric conditions (see Fig. 7). To prevent the fitted y values from clustering at the boundary values of $\pm 1\ \mathrm{atm}^{-1}$, we introduced a smooth penalty function—illustrated in Fig. 6(b)—into the residuals during optimization. As shown in Fig. 6(a), the resulting y values are evenly distributed within $[0, 1]$ and $[-1, 0]$, satisfying both the sum rule and the boundary constraints. For spectral lines with larger J, the distribution of y becomes more scattered, likely due to stronger line-mixing effects.

The simulation of the absorption coefficient for the methane $2\nu_3$ band serves as both a key application and a starting point of this work. As a straightforward demonstration, the parameters listed in Table 1 were converted to air-broadened values (available in the supplementary materials), and the full-band absorption cross-section was simulated under standard atmospheric conditions (pressure: 1 atm, temperature: 296 K, methane concentration: 2 ppm). For comparison, the absorption cross-section calculated using HITRAN2020 under the same conditions is also presented, along with the difference between the two results. The absorption cross section for methane, as simulated at 1 atm, displays clear discrepancies when compared to the extrapolated data derived from our findings. These differences are notably attributed to the enhanced precision in the spectral line intensity and line shape parameters in our analysis compared to those employed in HITRAN2020.

Examples of global fits

This section presents several examples of measured CRDS spectra and global fit results to demonstrate output quality. These results include: the R(0) singlet, without line mixing or symmetry constraints; the R(4) manifold, crucial for satellite observation of atmospheric methane; and the R(10) manifold, the most challenging one in this work, which consists of eleven closely spaced lines. These examples highlight the effectiveness of our global fit strategy. Results for other manifolds not shown here are available in the supplementary materials.

Fig. 8 shows the fit results for the R(0) transition at located at 6015.663827 cm^{-1}. The CRDS spectra, measured at 10 (green), 20 (orange), and 50 (red) kPa, cover the wavenumber range 6015.28–6015.94 cm^{-1}. Seven adjacent background transitions are marked by black short vertical lines in the upper panel, with the target transition highlighted in red. The residuals in the lower panel show background contributions in light gray for comparison. Because the R(0) manifold consists of a single line, no line mixing effects are considered. The W-shaped structures in the residuals (a) are due to an inadequate line-shape model, which we were able to correct using the HT profile (b). Using the clean residuals from the HT profile model, we estimate the CRDS noise level and the signal-to-noise ratio (SNR) of the spectra. For the 20 kPa spectra, SNR = $(\alpha_{\max} - \alpha_{\min})/\sigma \approx 952$, where $\alpha_{\max}$ and $\alpha_{\min}$ are the maximum and minimum absorption coefficients, respectively, and $\sigma \approx 1.2 \times 10^{-10}\mathrm{cm}^{-1}$ is the residual standard deviation.

Table 2
Error budget (k = 1) of the SDV and first-order lime mixing parameters of the R0-1 transition (6015.663827 cm^{-1}) (unit: percentage, %).

	Source	$u_r(\gamma_0)$ %	$u_r(\delta_0)$ %	$u_r(\gamma_2)$ %	$u_r(\delta_2)$ %
Type A	Statistical	0.02	0.10	0.33	9.65
Type B	Concentration	0.25	0.25	0.25	0.25
	Temperature	≤0.01	≤0.01	≤0.01	≤0.01
	Pressure	0.01	0.01	0.01	0.01
	Line-Shape	0.06	0.05	6.27	2.58
	Total	0.3	0.3	6	10

Fig. 9 shows the fit for the R(4) transition, with spectra spanning 6056.76 to 6057.43 cm^{-1}, and the reference transition at 6057.079461 cm^{-1}. The R(4) manifold is also highlighted as an example in the flow chart (Fig. 4). This transition consists of four target lines, with line mixing effects and symmetry constraints incorporated into the fitting process, as detailed in Section 2. The symmetry species of the target transitions are labeled in the upper panel for reference. The R(4) window is widely used in atmospheric applications, particularly for methane detection, because of its isolation from other transitions of water vapor and other atmospheric gases. Consequently, the present, high-precision parameter set for this region, which includes speed dependence and line mixing effects, is crucial for relevant applications. In our demonstration, the residuals remain below 0.5%, indicating a high-quality fit.

The R(10) manifold, as the most challenging example, is shown in Fig. 10. Earlier, we outlined the global fitting strategy, where accurate line assignments are critical for interpreting the complicated spectrum of methane. Line assignments reveal symmetry, which introduces additional constraints to promote reliable fitting outcomes. We determined the assignment for R(10) by juxtaposing theoretical predictions from Nikitin et al. [21] with empirical energy levels from MARVEL [22] and integrated saturation dip values. The fitting results also serve to validate the accuracy of the line assignment. The fit includes 11 lines spanning from 6114.26 cm^{-1} to 6114.93 cm^{-1}. Eight of these lines are closely spaced and overlap on both sides, merging into two major peaks, while the remaining three lines are positioned in between. During this assessment, we discovered a discrepancy in the spectral line assignment for R10-6, which prevented further assignment efforts, as documented in Table 1. For this transition, no symmetry constraints were applied, i.e. δ_0(R10-6) and δ_2(R10-6) are free parameters.

Uncertainty of parameters

In this section we examine the uncertainties associated with our spectroscopic parameters derived from fits of the SDV and first-order LM models to the CRDS spectrum. The uncertainty analysis for the R0-1 transition (6015.663827 cm^{-1}) is presented here as an example, because the inter-parameter coupling is less complicated in the R(0) manifold. A comprehensive uncertainty analysis is summarized in Table 2. The statistical uncertainty is retrieved from the standard deviation of around 100 individual fit outputs as illustrated. The uncertainty of the temperature measurement is ≈10 mK 2, the corresponding contribution to type B uncertainty is less than 0.01 K according to the temperature dependence of coefficients:

$$\gamma(T_0) = \gamma(T)\left(\frac{T}{T_0}\right)^n, \qquad \delta(T_0) = \delta(T)\left(\frac{T}{T_0}\right)^\eta, \tag{6}$$

where $T = 298\ \mathrm{K} \pm 10\ \mathrm{mK}$ is the nominal experimental temperature, $T_0 = 296$ K is the reference temperature, and $n = 0.86(7)$ is the temperature

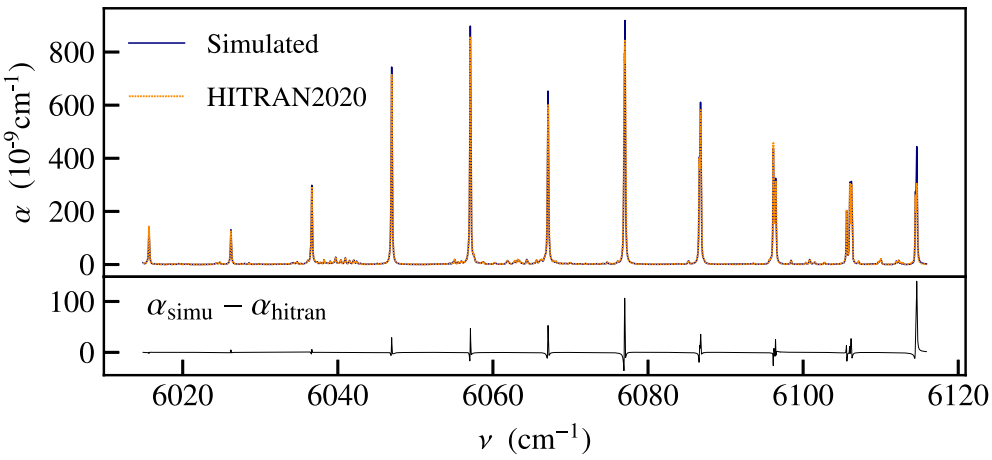

Fig. 7. Simulated absorption coefficient spectrum under standard atmospheric conditions (temperature: 296 K, pressure: 1 atm, methane concentration: 2 ppm, air broadening) using the line shape parameters measured in this work, compared with results from HITRAN2020 under the same conditions. The lower panel shows the difference between the two spectra.

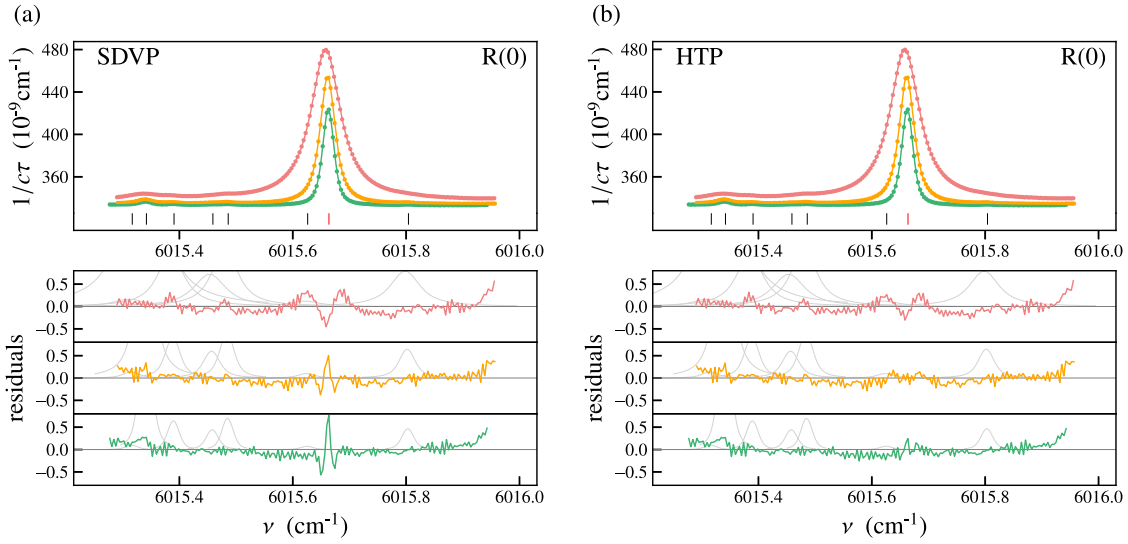

Fig. 8. CRDS spectra and global fit results for the R(0) transition at 6015.663827 cm^{-1}. (a) fit using SDVP, Vertical lines in the upper panel mark the positions of transitions: target lines (red) and background lines (gray). Different colors correspond to different experimental pressures: 10 kPa (green), 20 kPa (orange), and 50 kPa (red). The residuals for each fit are shown in the lower panel. Background line profiles are also plotted with the residuals at each pressure (light gray). (b) fit using HT profile, same schema as (a).

exponent [14]. The sample gas used in the CRDS measurement is a mixture of $^{12}CH_4$ and N_2. The amount fraction of $^{12}CH_4$ is 2.005 ppm with a relative uncertainty of 0.25%, resulting in a 0.25% systematic uncertainty. Line-shape uncertainties are estimated by comparing the SDVP fit results with those of the HTP model. The total uncertainties for γ_0, δ_0, γ_2, and δ_2 are estimated to be 0.3%, 0.3%, 6%, and 10%, respectively. The relative statistical and line-shape uncertainties are particularly significant for δ_2, as this parameter is too small and cannot be accurately determined through global fitting. In contrast to the HTP model, the γ_2 value specified by the SDV is greater, which is logical because the HTP model also accounts for the speed-dependent u_{VC}. Both this parameter and γ_2 contribute to line narrowing, thereby leading to an interaction and competition between these parameters. As a result, the error due to line shape for γ_2 is significantly larger than the statistical error.

Pressure broadening and shift coefficients

Several research groups have reported pressure broadening and shift coefficients for $2\nu_3$ band transitions. Devi et al. [15] measured air-broadening and shift coefficients for several hundred $2\nu_3$ transitions, covering most lines studied here. The SDVP model with relaxation matrix element coefficients was used in their work. Earlier, Nikitin et al. reported broadening and shift coefficients for methane transitions in the 5550–6236 cm^{-1} region in N_2 and O_2, using standard Voigt profile. Brown et al. [30] estimated broadening coefficients as a function of J''. Fig. 11 presents a systematic comparison of air-broadening coefficients. We converted our N_2-broadening coefficients to air-broadening using the relation:

$$\gamma_0^{air} = 0.79\gamma_0^{N_2} + 0.21\gamma_0^{O_2}, \tag{7}$$

with polynomial parameters for $\gamma_0^{O_2}$ from Lyulin et al. [13]:

$$\gamma_0^{O_2} = 0.0595 + 1.56 \times 10^{-3}|m| - 2.01 \times 10^{-4}|m|^2. \tag{8}$$

where $|m|$ is the lower state rotational quantum number ($m = -J$ for P-branch, $m = J$ for Q-branch and $m = J+1$ for R-branch). The values are grouped by transition symmetry: red for A1↔A2, blue for F1↔F2, and green for E↔E. The nitrogen pressure shifting coefficients are similarly scaled as $\delta_0^{air} = 0.79\delta_0^{N_2} + 0.21\delta_0^{O_2}$, again utilizing $\delta_0^{O_2} = -0.0105$ as provided by Lyulin et al. while values of $Y_n^{N_2}$ for the measured CH_4-N_2 system are converted for CH_4- air through multiplication by 0.985,

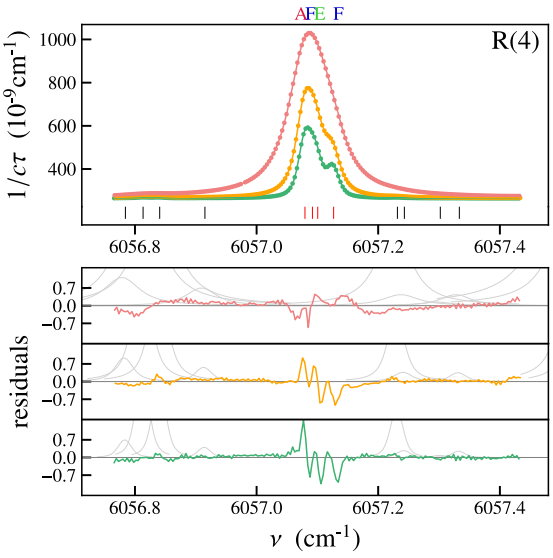

Fig. 9. CRDS spectra and global fit results for the R(4) transition at 6057.1 cm^{-1} using the SDV and first-order line mixing model. The same scheme as in Fig. 8 is used. Additionally, the transition symmetries are marked above the upper panel, F for F1↔F2, A for A1↔A2, and E for E↔E.

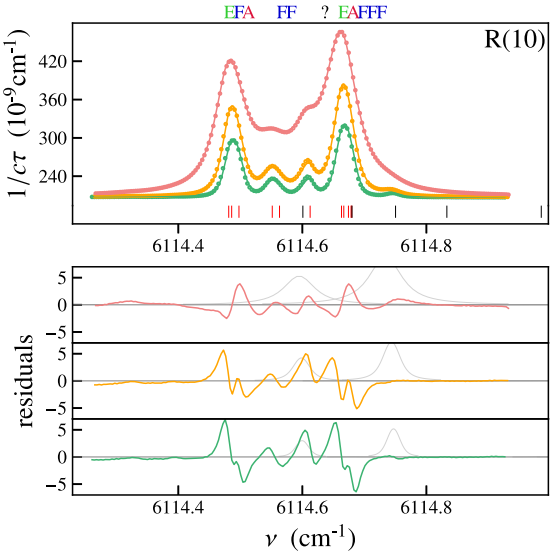

Fig. 10. CRDS spectra and global fit result of some R-branch multiplets in $^{12}CH_4$ $2\nu_3$ band. Different colors represent different experimental pressures: 10 kpa (blue), 20 kpa (green), 50 kpa (orange). The respective residuals are shown in the bottom panel. Vertical lines in the background indicate the positions of individual transitions: target lines (red), background lines (gray). The profiles of background lines are plotted along with residuals in corresponding pressures.

as shown in Tran et al. for the $2\nu_3$ band [31]. The $\gamma_0^{O_2}$ values presented here are derived from the polynomial approximation framework proposed by Lyulin et al. [13], which incorporates both optimally fitted coefficients and their corresponding confidence intervals. The conversion process to γ_0^{air} introduces an associated uncertainty ranging from approximately 0.3% to 1.6%. In the case of $\delta_0^{O_2}$, Lyulin et al. reported a mean value accompanied by a standard error of 0.0029 $cm^{-1}atm^{-1}$. This propagation of error translates to an estimated uncertainty of 3% to 10% during the conversion to δ_0^{air}, further emphasizing the need for careful consideration of these systematic biases in subsequent data interpretation.

For transitions ranging from R(0) to R(6) concerning γ_0 values, the relative discrepancies between our findings and those in the works

Table 3
N_2-broadening and shift coefficients of the R(9) line.

Line	Ref. [15]	Ref. [7]	This work
	$\gamma_0^{N_2}$ ($cm^{-1}atm^{-1}$)		
R9-1	0.05075(1)	0.054185(31)	0.05122(2)
R9-2	0.05075(1)	0.054185(31)	0.05285(2)
	$\delta_0^{N_2}$ ($cm^{-1}atm^{-1}$)		
R9-1	−0.01115(1)	−0.011557(59)	−0.0221(3)
R9-2	−0.01115(1)	−0.011557(59)	−0.0221(3)

Table 4
N_2-broadening and shift coefficients of the R(10) line.

Line	Ref. [15]	Ref. [13]	This work
	$\gamma_0^{N_2}$ ($cm^{-1}atm^{-1}$)		
R10-1	0.06387(46)	–	0.04633(1)
R10-2	0.03811(8)	0.0430(3)	0.04492(2)
R10-3	0.05252(8)	0.0527(4)	0.06120(3)
R10-4	0.07604(15)	–	0.06274(2)
R10-6	0.03488(6)	–	0.03954(F)
R10-10	0.05748(6)	0.0487(2)	0.06062(4)
	$\delta_0^{N_2}$ ($cm^{-1}atm^{-1}$)		
R10-1	−0.01183(8)	–	−0.00895(2)
R10-2	−0.00850(6)	−0.0078(3)	−0.01691(1)
R10-3	−0.01296(6)	−0.0059(4)	−0.01972(2)
R10-4	−0.01659(6)	–	−0.01691(1)
R10-6	−0.00278(F)	–	−0.014873(9)
R10-10	−0.00882(5)	−0.0135(3)	−0.01691(1)

of Devi et al. as well as the majority of Nikitin et al. remain under 10%, as depicted in Fig. 11. Regarding δ_0, the measured values for the transitions R(0), R(1), R(4), and R(6) align with those of Devi et al. within a margin of 1%–2%, as illustrated in Fig. 12. For transitions with lower J'', our results generally align well with those of Devi et al. and Nikitin et al. [3,15], with values scattered about the estimates from Brown et al. However, for higher J'', while the mean values still align with the dashed lines, the data points become more discrete, and discrepancies become more pronounced. This is especially evident for R(9) and R(10) transitions. These two manifolds are relatively difficult to fit, resulting in larger residuals and more scattered outcomes. Therefore, we have compiled existing literature results in Tables 3 and 4 for comparison with the results of this work. In addition, Vasilchenko et al. [11] employed a similar multispectral fitting approach based on the HT profile; the corresponding parameters are also compared in Table 5. The disparity in the line function applied results in notable variations in the line parameters derived by the two studies.

The objective of our research is to advance the existing line shape parameters in the HITRAN2024 database while supplying crucial experimental reference data to refine satellite remote sensing and terrestrial observations of methane. Consequently, we convert our data from nitrogen-broadening to air-broadening using Eqs. (7) and (8). The complete line list, associated with both speed-dependent Voigt and Voigt profiles with first-order line-mixing, is available in the Supplementary files. The full landscape of the fitting results for R(0) - R(10) manifolds across 10–50 kPa pressures is also provided in the Supplementary files.

5. Conclusion and outlook

This study presents high-precision measurements of the 1.64 μm methane spectrum, focusing on the R(0) to R(10) manifolds of the $2\nu_3$ band under N_2-broadened conditions. The substantial spectral congestion present in methane renders the measurement and prediction of its individual line parameters technically arduous. The spectral overlap leads to correlation between fitted parameters, increasing the uncertainty of line-by-line parameter measurements when compared to comparable results for more isolated transitions. Aiming to tackle

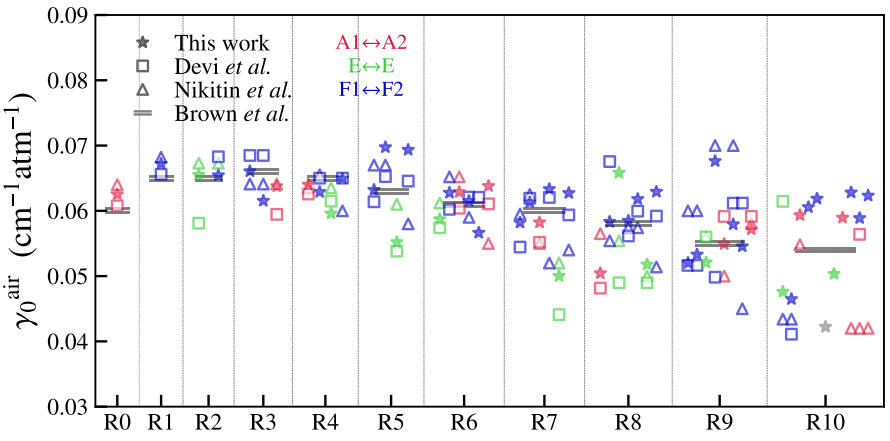

Fig. 11. Air-broadening coefficients γ_0^{air} (cm^{-1}atm^{-1}), measured in this study and compared with literature values. Markers: Solid stars (this work), hollow squares (Devi et al.), hollow triangles (Nikitin et al.), and dashed lines (Brown et al.). Color coding by transition symmetry: Red (A1↔A2), blue (F1↔F2), green (E↔E). An inconsistency in R(10) line lists and missing assignments is noted.

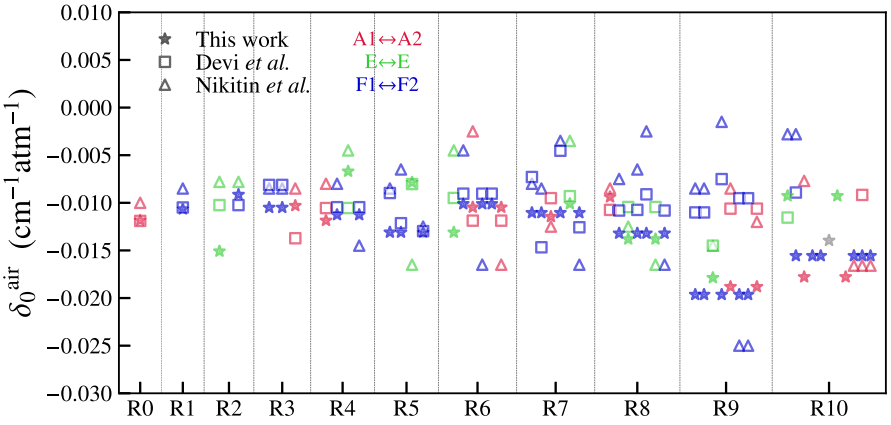

Fig. 12. Air-shift coefficients δ_0^{air} (cm^{-1}atm^{-1}) measured in this study and compared with literature values. Markers: Solid stars (this work), hollow squares (Devi et al.), hollow triangles (Nikitin et al.), Same color scheme are used for transition symmetry.

Table 5
The line shape parameters retrieved from this work and those from Vasilchenko *et al.* [11] using the HT profile for the R(6) manifold.

Parameter		R(6) Transition					
		R6-1	R6-2	R6-3	R6-4	R6-5	R6-6
γ_0	Ref.	0.06378(17)	0.055263(85)	0.063498(46)	0.055591(59)	0.043340(30)	0.059516(41)
	Ours	0.05822(6)	0.06335(9)	0.06349(2)	0.06176(2)	0.05559(8)	0.06466(3)
δ_0	Ref.	−0.02302(14)	−0.00524(08)	−0.01014(02)	−0.00673(03)	−0.01729(04)	−0.00795(02)
	Ours	−0.01379(5)	−0.01001(3)	−0.01047(5)	−0.01001(3)	−0.01001(3)	−0.01047(5)
γ_2	Ref.	0.01697(28)	0.00011(30)	0.01246(20)	0.00191(34)	0.00619(33)	0.00980(15)
	Ours	0.00940(−)	0.008255(8)	0.01116(1)	0.00938(4)	0.005559(8)	0.011436(8)
δ_2	Ref.	−0.00494(13)	0.00746(22)	−0.00426(13)	−0.00432(71)	−0.00918(28)	0.001293(06)
	Ours	−0.00018(3)	−0.00080(4)	−0.00216(6)	−0.00080(4)	−0.00080(4)	−0.00216(6)
y	Ref.	0	−0.3412(48)	−0.1611(27)	0.4297(38)	0.0977(56)	0.0434(25)
	Ours	0	0.256(2)	0.233(1)	0.525(2)	−0.781(1)	−0.233(1)
ν_{vc}	Ref.	0	0	1.433(31)	0.476(85)	0	0.58(31)
	Ours	–	–	–	–	–	–
η	Ref.	0.171(27)	0.080(66)	0.363(17)	0.058(48)	0.775(26)	0
	Ours	–	–	–	–	–	–

these complexities and enhance methane databases, the experimental methodology was meticulously organized into a tripartite framework to manage spectral complications that occur over a wide range of pressure conditions. In the first phase, methane line positions were determined using saturation absorption spectroscopy, thereby establishing a foundational zero-pressure line-position reference for subsequent analyses. The second phase, conducted in collaboration with NIST and DLR, involved low-pressure (nearly Doppler-broadened) spectral measurements on samples of well-characterized methane amount fraction, to extract accurate line intensities. The third phase, led by USTC, targeted higher-pressure absorption spectroscopy to resolve collision-induced broadening and line-mixing effects, where spectral overlap posed significant analytical challenges. By integrating position data from phase one, line intensities from phase two, and pressure-dependent line profiles from phase three into a unified global fitting model including speed dependence and line mixing effects, we achieved a self-consistent framework for spectral parameter retrieval. This iterative process enabled a mutual validation approach including: high-pressure line-shape feedback which refined residual deviations from Doppler broadening effects in low-pressure analyses, while low-pressure constraints enhanced the disentanglement of strongly overlapping spectral features at elevated pressures. The synergy between experimental phases and international collaboration ensured robust determination of N_2-broadening coefficients and intensity ratios, resolving discrepancies in prior studies and providing new benchmarks for updating the HITRAN024 methane spectral data.

This three-phase experimental approach, once effectively implemented, highlights its proven capability to realize precise spectroscopic parameter retrievals in congested molecular spectra. We anticipate that future applications will address broader spectral sections of methane and various collisional broadening partners such as O_2, H_2, and He to better capture the atmospheric variations found in both terrestrial and planetary settings. Additionally, the incorporation of more advanced line-shape models or the adoption of a full-matrix line-mixing model is anticipated to further improve the accuracy of methane spectral data retrievals, thus forming a strong physics-based foundation for precise atmospheric methane observations. By aligning laboratory-level accuracy with the complexities of real-world atmospheres, this research reinforces the importance of molecular spectroscopy as an essential tool for tackling new scientific challenges within the Earth system and beyond, including refining climate simulations and understanding exoplanetary atmospheres.

CRediT authorship contribution statement

R.-H. Yin: Writing – original draft, Visualization, Validation, Software, Funding acquisition, Formal analysis, Data curation, Conceptualization. **J.-K. Li:** Writing – original draft, Validation, Methodology, Investigation, Data curation, Conceptualization. **J. Wang:** Writing – original draft, Investigation, Data curation, Conceptualization. **A.-W. Liu:** Validation, Resources, Conceptualization. **Z.D. Reed:** Writing – review & editing, Validation, Methodology, Conceptualization. **J.T. Hodges:** Writing – review & editing, Validation, Methodology, Conceptualization. **M. Birk:** Validation, Methodology. **Y. Tan:** Writing – review & editing, Writing – original draft, Visualization, Validation, Supervision, Software, Resources, Project administration, Methodology, Investigation, Funding acquisition, Formal analysis, Data curation, Conceptualization. **S.-M. Hu:** Writing – review & editing, Validation, Supervision, Project administration, Conceptualization.

Declaration of competing interest

The authors declare the following financial interests/personal relationships which may be considered as potential competing interests: Yan Tan reports financial support was provided by the Ministry of Science and Technology of China. If there are other authors, they declare that they have no known competing financial interests or personal relationships that could have appeared to influence the work reported in this paper. Identification of certain commercial equipment, instruments, software, or materials does not imply recommendation or endorsement by the National Institute of Standards and Technology, nor does it imply that the products identified are necessarily the best available for the purpose.

Acknowledgments

This work was supported by the Ministry of Science and Technology of China (Grant No. 2022YFF0606500), and the National Natural Science Foundation of China (Grant Nos. 12393822, 12393825).

Appendix A. Supplementary data

Supplementary material related to this article can be found online at https://doi.org/10.1016/j.jqsrt.2025.109588.

Data availability

No data was used for the research described in the article.

References

[1] Saunois M, Martinez A, Poulter B, Zhang Z, Raymond P, Regnier P, Canadell JG, Jackson RB, Patra PK, Bousquet P, Ciais P, Dlugokencky EJ, Lan X, Allen GH, Bastviken D, Beerling DJ, Belikov DA, Blake DR, Castaldi S, Crippa M, Deemer BR, Dennison F, Etiope G, Gedney N, Höglund-Isaksson L, Holgerson MA, Hopcroft PO, Hugelius G, Ito A, Jain AK, Janardanan R, Johnson MS, Kleinen T, Krummel P, Lauerwald R, Li T, Liu X, McDonald KC, Melton JR, Mühle J, Müller J, Murguia-Flores F, Niwa Y, Noce S, Pan S, Parker RJ, Peng C, Ramonet M, Riley WJ, Rocher-Ros G, Rosentreter JA, Sasakawa M, Segers A, Smith SJ, Stanley EH, Thanwerdas J, Tian H, Tsuruta A, Tubiello FN, Weber TS, van der Werf G, Worthy DE, Xi Y, Yoshida Y, Zhang W, Zheng B, Zhu Q, Zhu Q, Zhuang Q. Global methane budget 2000–2020. Earth Syst Sci Data Discuss 2024;2024:1–147. http://dx.doi.org/10.5194/essd-2024-115.

[2] Ehret G, Bousquet P, Pierangelo C, Alpers M, Millet B, Abshire JB, Bovensmann H, Burrows JP, Chevallier F, Ciais P, Crevoisier C, Fix A, Flamant P, Frankenberg C, Gibert F, Heim B, Heimann M, Houweling S, Hubberten HW, Jöckel P, Law K, Löw A, Marshall J, Agusti-Panareda A, Payan S, Prigent C, Rairoux P, Sachs T, Scholze M, Wirth M. MERLIN: A French-German space lidar mission dedicated to atmospheric methane. Remote Sens 2017;9:1–29. http://dx.doi.org/10.3390/rs9101052.

[3] Nikitin A, Lyulin O, Mikhailenko S, Perevalov V, Filippov N, Grigoriev I, Morino I, Yoshida Y, Matsunaga T. GOSAT-2014 methane spectral line list. J Quant Spectrosc Radiat Transfer 2015;154:63–71. http://dx.doi.org/10.1016/j.jqsrt.2014.12.003.

[4] Gordon I, Rothman L, Hargreaves R, Hashemi R, Karlovets E, Skinner F, Conway E, Hill C, Kochanov R, Tan Y, Wcisło P, Finenko A, Nelson K, Bernath P, Birk M, Boudon V, Campargue A, Chance K, Coustenis A, Drouin B, Flaud J-M, Gamache R, Hodges J, Jacquemart D, Mlawer E, Nikitin A, Perevalov V, Rotger M, Tennyson J, Toon G, Tran H, Tyuterev V, Adkins E, Baker A, Barbe A, Canè E, Császár A, Dudaryonok A, Egorov O, Fleisher A, Fleurbaey H, Foltynowicz A, Furtenbacher T, Harrison J, Hartmann J-M, Horneman V-M, Huang X, Karman T, Karns J, Kassi S, Kleiner I, Kofman V, Kwabia-Tchana F, Lavrentieva N, Lee T, Long D, Lukashevskaya A, Lyulin O, Makhnev V, Matt W, Massie S, Melosso M, Mikhailenko S, Mondelain D, Müller H, Naumenko O, Perrin A, Polyansky O, Raddaoui E, Raston P, Reed Z, Rey M, Richard C, Tóbiás R, Sadiek I, Schwenke D, Starikova E, Sung K, Tamassia F, Tashkun S, Auwera JV, Vasilenko I, Vigasin A, Villanueva G, Vispoel B, Wagner G, Yachmenev A, Yurchenko S. The HITRAN2020 molecular spectroscopic database. J Quant Spectrosc Radiat Transfer 2022;277:107949. http://dx.doi.org/10.1016/j.jqsrt.2021.107949.

[5] Gordon IE, Rothman LS, Hill C, Kochanov RV, Tan Y, Bernath PF, Birk M, Boudon V, Campargue A, Chance KV, Drouin BJ, Flaud JM, Gamache RR, Hodges JT, Jacquemart D, Perevalov VI, Perrin A, Shine KP, Smith MAH, Tennyson J, Toon GC, Tran H, Tyuterev VG, Barbe A, Császár AG, Devi VM, Furtenbacher T, Harrison JJ, Hartmann JM, Jolly A, Johnson TJ, Karman T, Kleiner I, Kyuberis AA, Loos J, Lyulin OM, Massie ST, Mikhailenko SN, Moazzen-Ahmadi N, Müller HSP, Naumenko OV, Nikitin AV, Polyansky OL, Rey M, Rotger M, Sharpe SW, Sung K, Starikova E, Tashkun SA, Auwera J Vander, Wagner G, Wilzewski J, Wcisło P, Yu S, Zak EJ. The hitran2016 molecular spectroscopic database. 2017;203:3–69. http://dx.doi.org/10.1016/j.jqsrt.2017.06.038.

[6] Delahaye T, Maxwell SE, Reed ZD, Lin H, Hodges JT, Sung K, Devi VM, Warneke T, Spietz P, Tran H. Precise methane absorption measurements in the 1.64 μm spectral region for the MERLIN mission. J Geophys Res: Atmos 2016;121:7360–70. http://dx.doi.org/10.1002/2016JD025024.

[7] Yang L, Lin H, Plimmer MD, Feng XJ, Zhang JT. Lineshape test on overlapped transitions (R9F1, R9F2) of the $2\nu_3$ band of $^{12}CH_4$ by frequency-stabilized cavity ring-down spectroscopy. J Quant Spectrosc Radiat Transfer 2018;210:82–90. http://dx.doi.org/10.1016/j.jqsrt.2018.02.019.

[8] Nikitin AV, Boudon V, Wenger C, Albert S, Brown LR, Bauerecker S, Quack M. High resolution spectroscopy and the first global analysis of the tetradecad region of methane $^{12}CH_4$. Phys Chem Chem Phys 2013;15:10071–93. http://dx.doi.org/10.1039/c3cp50799h.

[9] Nikitin AV, Chizhmakova IS, Rey M, Tashkun SA, Kassi S, Mondelain D, Campargue A, Tyuterev VG. Analysis of the absorption spectrum of $^{12}CH_4$ in the region 5855-6250 cm^{-1} of the $2\nu_3$ band. J Quant Spectrosc Radiat Transfer 2017;203:341–8. http://dx.doi.org/10.1016/j.jqsrt.2017.05.014.

[10] Malina E, Veihelmann B, Buschmann M, Deutscher NM, Feist DG, Morino I. On the consistency of methane retrievals using the total carbon column observing network (TCCON) and multiple spectroscopic databases. Atmos Meas Tech 2022;15:2377–406. http://dx.doi.org/10.5194/amt-15-2377-2022.

[11] Vasilchenko S, Delahaye T, Kassi S, Campargue A, Armante R, Tran H, Mondelain D. Temperature dependence of the absorption of the R(6) manifold of the 2ν 3 band of methane in air in support of the MERLIN mission. J Quant Spectrosc Radiat Transfer 2023;298:108483. http://dx.doi.org/10.1016/j.jqsrt.2023.108483.

[12] Frankenberg C, Warneke T, Butz A, Aben I, Hase F, Spietz P, Brown LR. Pressure broadening in the 2ν3 band of methane and its implication on atmospheric retrievals. Atmos Chem Phys 2008;8:5061–75. http://dx.doi.org/10.5194/acp-8-5061-2008.

[13] Lyulin OM, Nikitin AV, Perevalov VI, Morino I, Yokota T, Kumazawa R, Watanabe T. Measurements of N_2- and O_2-broadening and shifting parameters of methane spectral lines in the 5550-6236 cm^{-1} region. J Quant Spectrosc Radiat Transfer 2009;110:654–68. http://dx.doi.org/10.1016/j.jqsrt.2009.02.012.

[14] Lyulin O, Perevalov V, Morino I, Yokota T, Kumazawa R, Watanabe T. Measurements of self-broadening and self-pressure-induced shift parameters of the methane spectral lines in the 5556-6166 cm^{-1} range. J Quant Spectrosc Radiat Transfer 2011;112:531–9. http://dx.doi.org/10.1016/j.jqsrt.2010.10.010.

[15] Devi VM, Benner DC, Sung K, Crawford TJ, Yu S, Brown LR, Smith MAH, Mantz AW, Boudon V, Ismail S. Self- and air-broadened line shapes in the $2\nu_3$ P and R branches of $^{12}CH_4$. J Mol Spectrosc 2015;315:114–36. http://dx.doi.org/10.1016/j.jms.2015.05.003.

[16] Delahaye T, Ghysels M, Hodges JT, Sung K, Armante R, Tran H. Measurement and modeling of air-broadened methane absorption in the MERLIN spectral region at low temperatures. J Geophys Res: Atmos 2019;124:3556–64. http://dx.doi.org/10.1029/2018JD028917.

[17] Reed ZD, Birk M, Tan Y, Cecelski C, Wagner G, Hu S-M, Long DA, Yin R-H, Hodges JT. Mult-laboratory measurements of $^{12}CH_4$ $2\nu_3$-band line parameters, Part *I*: Line intensities with relative combined uncertainties at the permille level. 2025.

[18] Votava O, Kassi S, Campargue A, Romanini D. Comb coherence-transfer and cavity ring-down saturation spectroscopy around 1.65 μm: khz-accurate frequencies of transitions in the $2\nu_3$ band of $^{12}CH_4$. Phys Chem Chem Phys 2022;24:4157–73. http://dx.doi.org/10.1039/D1CP04989E.

[19] Wang J, Sun YR, Tao L-G, Liu A-W, Hu S-M. Communication: Molecular near-infrared transitions determined with sub-khz accuracy. J Chem Phys 2017;147:091103. http://dx.doi.org/10.1063/1.4998763.

[20] Wang J, Hu C-L, Liu A-W, Sun Y, Tan Y, Hu S-M. Saturated absorption spectroscopy near 1.57 μm and revised rotational line list of ^{12}c16O. J Quant Spectrosc Radiat Transfer 2021;270:107717. http://dx.doi.org/10.1016/j.jqsrt.2021.107717.

[21] Nikitin AV, Boudon V, Wenger C, Albert S, Brown LR, Bauerecker S, Quack M. High resolution spectroscopy and the first global analysis of the tetradecad region of methane $^{12}CH_4$. Phys Chem Chem Phys 2013;15:10071–93. http://dx.doi.org/10.1039/c3cp50799h.

[22] Kefala K, Boudon V, Yurchenko SN, Tennyson J. Empirical rovibrational energy levels for methane. J Quant Spectrosc Radiat Transfer 2024;316:108897. http://dx.doi.org/10.1016/j.jqsrt.2024.108897.

[23] Liang H, Tan Y, Hu C-L, Nie Z-L, Liu A-W, Sun YR, Wang J, Hu S-M. Cavity-enhanced absorption and dispersion spectroscopy of the 1238-nm line of h_2. Phys Rev A 2024;110:042817. http://dx.doi.org/10.1103/PhysRevA.110.042817.

[24] Yang L, Lin H, Plimmer MD, Feng XJ, Ma YJ, Luo JT, Luo JF, Zhang JT. Measurement of the spectral line positions in the $2\nu_3$ R6 manifold of methane. J Quant Spectrosc Radiat Transfer 2020;245. http://dx.doi.org/10.1016/j.jqsrt.2020.106888.

[25] Ciuryło R, Pine A, Szudy J. A generalized speed-dependent line profile combining soft and hard partially correlated dicke-narrowing collisions. J Quant Spectrosc Radiat Transfer 2001;68:257–71. http://dx.doi.org/10.1016/S0022-4073(00)00024-8.

[26] Ngo N, Lisak D, Tran H, Hartmann J-M. An isolated line-shape model to go beyond the voigt profile in spectroscopic databases and radiative transfer codes. J Quant Spectrosc Radiat Transfer 2013;129:89–100. http://dx.doi.org/10.1016/j.jqsrt.2013.05.034.

[27] Ngo N, Lisak D, Tran H, Hartmann J-M. Erratum to an isolated line-shape model to go beyond the voigt profile in spectroscopic databases and radiative transfer codes [j. quant. spectrosc. radiat. transf. 129 (2013) 89-100]. J Quant Spectrosc Radiat Transfer 2013;129:89–100. http://dx.doi.org/10.1016/j.jqsrt.2013.10.016.

[28] Rosenkranz P. Shape of the 5mm oxygen band in the atmosphere. IEEE Trans Antennas and Propagation 1975;23:498–506. http://dx.doi.org/10.1109/TAP.1975.1141119.

[29] Pine A. N2 and ar broadening and line mixing in the p and r branches of the v3 band of ch4. J Quant Spectrosc Radiat Transfer 1997;57(2):157–76. http://dx.doi.org/10.1016/S0022-4073(96)00130-6.

[30] Brown L, Sung K, Benner D, Devi V, Boudon V, Gabard T, Wenger C, Campargue A, Leshchishina O, Kassi S, Mondelain D, Wang L, Daumont L, Régalia L, Rey M, Thomas X, Tyuterev VG, Lyulin O, Nikitin A, Niederer H, Albert S, Bauerecker S, Quack M, O'Brien J, Gordon I, Rothman L, Sasada H, Coustenis A, Smith M, Carrington T, Wang X-G, Mantz A, Spickler P. Methane line parameters in the HITRAN2012 database. J Quant Spectrosc Radiat Transfer 2013;130:201–19. http://dx.doi.org/10.1016/j.jqsrt.2013.06.020.

[31] Tran H, Hartmann JM, Toon G, Brown LR, Frankenberg C, Warneke T, Spietz P, Hase F. The $2\nu_3$ band of $^{12}CH_4$ revisited with line mixing: Consequences for spectroscopy and atmospheric retrievals at 1.67 μm. J Quant Spectrosc Radiat Transfer 2010;111(10):1344–56. http://dx.doi.org/10.1016/j.jqsrt.2010.02.015.